공학석사 학위논문

# 폴리디메틸실록산의 연속 레이저 열분해를 통한 투명 다기능 센서 구현

Transparent Multifunctional Sensor by

Successive Laser Pyrolysis of Polydimethylsiloxane

2023년 2월

서울대학교 대학원

기계공학부

이 재 군

# 폴리디메틸실록산의 연속 레이저 열분해를 통한 투명 다기능 센서 구현

Transparent Multifunctional Sensor by

Successive Laser Pyrolysis of Polydimethylsiloxane

지도교수 고 승 환

이 논문을 공학석사 학위논문으로 제출함

2022년 10월

서울대학교 대학원

기계공학부

이 재 군

이재군의 공학석사 학위논문을 인준함

2022년 12월

위 원 장 송 한 호 (인)

부위원장 고 승 환 (인)

위 원 도 형 록 (인)

# Abstract

Research about laser direct patterning (LDP) is widely progressed in selective and reversible laser doping, phase separation of polymer, laser sintering, and laser ablation because of its ease and efficiency of the process. Among LDP fields, research about laser induced graphene (LIG) which irradiates a laser on carbon rich materials in ambient atmosphere gets attention because produced graphene has porous property and high electrical conductivity. Mechanical sensors, chemical sensors, and energy devices can be fabricated based on the properties of LIG. However, LIG has some limits which are about a line width resolution and need an additional process to use transparent applications. In this research, we will introduce the successive laser pyrolysis (SLP) process of polydimethylsiloxane (PDMS) which can break the limits of LIG in a simple process and examine the performance of byproducts of SLP as strain, temperature, and gas sensors to confirm the possibility of substituting LIG. Consequently, byproducts of SLP composed of $SiO_2$, beta-SiC, and carbon materials can perform as a transparent multifunctional sensor and substitute the LIG from a long-term perspective.

**Keyword :** Polydimethylsiloxane, Laser direct patterning, Laser pyrolysis, Transparent sensor, Multifunctional sensor

**Student Number :** 2021-24532

# Table of Contents

# List of Figures

**Figure 10.** (a) XPS results of byproducts for various laser energy densities. (b) Atomic percentage differences of C and O atoms depending on laser energy density.

**Figure 11.** (a) Sample images for Raman spectroscopy. (b) Raman spectroscopy results of byproducts. (c) Peak ratios of Raman spectroscopy results.

**Figure 12.** Raman spectroscopy results of byproducts to explain the tendency of beta-SiC.

**Figure 13.** Hierarchical composition of byproducts.

**Figure 14.** (a) Strain response curve of byproducts depending on laser energy density. (b) Gauge factor (GF) at high and low strain.

**Figure 15.** (a) Minimum detectable strain of 5J/m sample. (b) Time dependent cyclic response of 5J/m sample. (c) Durability test of 5J/m sample at 30% strain.

**Figure 16.** (a) Temperature response curve of byproducts depending on laser energy density. (b) Sensitivity according to the temperature of fabricated sensors. (c) Durability test of 25J/m sample at cyclic conditions between 25 and 200°C.

**Figure 17.** (a) $NO_2$ gas response curve of byproducts depending on laser energy density. (b) Sensitivity of byproducts according to various concentrations of $NO_2$ gas. (c) Time constant $\tau_1$ about $NO_2$ concentrations.

**Figure 18.** Two-phase exponential decay model fitting curve between 10ppm $NO_2$ and (a) 5J/m byproducts, (b) 15J/m byproducts, and (c) 25J/m byproducts.

**Figure 19.** (a) Response curve of 5J/m sensor to various $NO_2$ concentrations. (b)

Response curve about with and without humidity.

**Figure 20.** (a) Full response curve between 5J/m byproducts and various gases. (b) The selectivity of $NO_2$ gas among various gases.

# Chapter 1. Introduction

## 1.1 Study Backgrounds

Nowadays, realizing transparent and multifunctional properties in one sensor is important because of its tremendous applications such as wearable electronics, E-skin, and soft robotics.[1] [2] [3] To fabricate these sensors, lots of research are being progressed. Among these investigations, laser direct patterning (LDP) method is adopted extensively because of the ease of processing.[4] [5] LDP, the technology processing various materials at room temperature and ambient pressure, is used in selective and reversible doping, phase separation of polymers, and sintering and ablation of nanomaterials.[6] [7] [8] More specifically, laser direct patterning (LIG), obtaining porous graphene by processing carbon rich materials using various wavelength lasers, is widely used in LDP application field to manufacture transparent and multifunctional sensor.[5] [9] [10] [11]

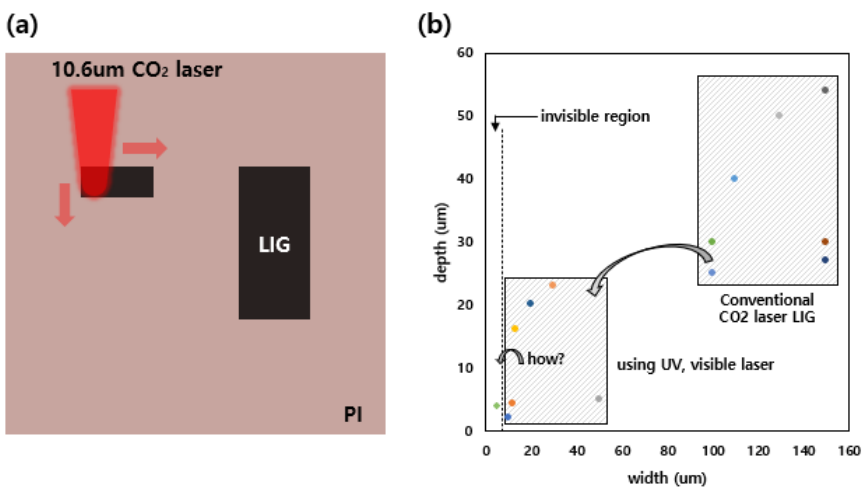


**Figure 1. (a) Concept of laser induced graphene (LIG) process. (b) Limit of LIG about line width.**

In general, LIG process is the conversion of a commercial carbon-rich films like

polyimide into 3D porous graphene under ambient conditions using 10.6um $CO_2$ laser as shown in Figure 1. (a). However, LIG method has some limitations in aspects of its process and final product for transparent applications. The first limitation is that for using generated graphene by LIG as a transparent purpose, additional processes are needed for transferring to transparent substrates such as eco-flex and polydimethylsiloxane (PDMS).[12] [13] Needs of additional processes result in increase of process time and cost. The second limitation is the line width fabricated by LIG can't achieve under 5~10um because of the high power of $CO_2$ lasers and the light absorbing property of materials.[14] [15] [16] Figure 1. (b) shows the process of development of line width as a result of LIG. Researchers tried to fabricate smaller line width compared to the product of $CO_2$ laser by using small power of UV and visible laser. Despite the researchers' efforts, it is hard to make line width under 10um with the latest techniques. If we develop a new process that realizes line width under 10um, we can use materials and area more efficiently and make highly transparent sensors.

## 1.2 Purpose of This Research

We build up the process named successive laser pyrolysis (SLP), machining transparent PDMS polymer, to solve the limitations of LIG.[17] At first, PDMS is biocompatible and transparent polymer which is widely used in bioengineering, organ-on-a-chip, microfluidic, and stretchable electronics.[18] [19] [20] SLP method utilizes a continuous wave 532nm wavelength laser and dark color initiator. More specifically, the initiator is marked on PDMS first and then the laser is scanned from that point. The rapid and successive pyrolysis of PDMS is occurred because of the higher laser absorption of the initiator.

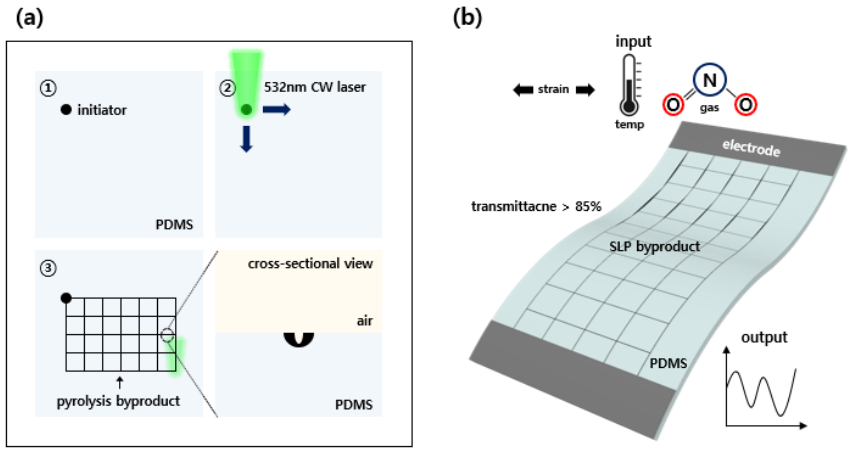


**Figure 2. (a) Flow of successive laser pyrolysis (SLP) process. (b) Schematic of SLP byproducts application as a transparent and multifunctional sensor.**

As a result of SLP, transparent final products can be fabricated on the hyaline substrate at a time. Furthermore, line width under 10um can be manufactured by modulating the laser power and the scan speed because of the high light transmittance of PDMS in the visible region. The mechanism of SLP is that the fast-heating rate of PDMS by laser causes the radical mechanism and suppresses the molecular mechanism which dominates relatively low temperature regions under 400°C.[17] [21] Radical and molecular mechanisms are representative pyrolysis mechanisms of PDMS. This phenomenon makes relatively low temperature pyrolysis of PMDS possible and generates byproducts composed of beta-SiC, and carbon materials like graphite and graphene. In this experiment, we will discuss various properties of SLP byproducts and evaluate the performances of byproducts as strain, temperature, and gas sensors. Figure 2. (a) shows the schematic of the SLP and we can verify the existence of the initiator. We can confirm that the cross-section of the byproduct looks like a trench shape. Figure 2. (b) shows the fabricated samples' application as a transparent and multifunctional sensor detecting strain, temperature, and gas based on the byproducts of SLP.

# Chapter 2. Experiment Preparation

## 2.1 PDMS Sample Fabrication Process

To develop a reliable SLP and applications, sophisticated PDMS samples are important. Figure 3 shows the steps of making PDMS samples.

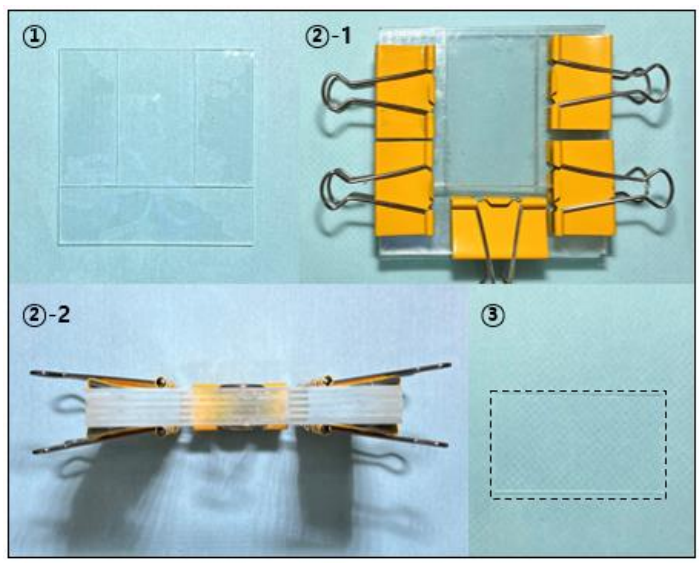


**Figure 3. Fabrication process of 1mm thickness PDMS using acrylic mold.**

Small differences in PDMS thickness can cause huge variations in byproducts as shown in Figure 4. (b). Therefore, we used acrylic molds which have high reliability than the spin coating known as having an edge-bead to fabricate 1mm thickness PDMS.[22] [23] The PDMS is prepared by mixing the resin and curing agent (Sylgard 184, Dow Corning) in a 10:1 weight ratio. The degassing process is progressed in a vacuum chamber. Degassed PDMS is poured into the acrylic mold which has a 1mm spacer. As a result of this method, reliable sensor results are acquired when we do the strain, temperature, and gas sensor performance tests.

## 2.2 Optic Set-up and the Result of Different Focal Length

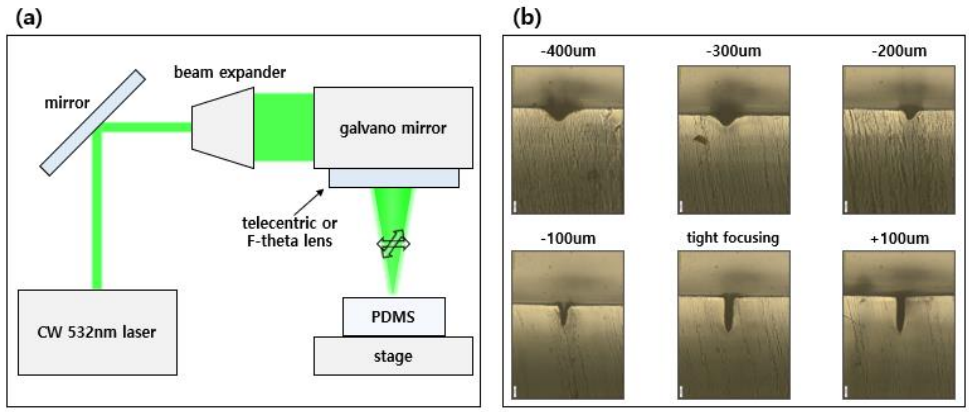


**Figure 4. (a) Laser optic system for the SLP. (b) Different width and depth of byproducts depending on laser focal length.**

Figure 4. (a) shows the Galvano-mirror based optical system for the SLP. We can control the experiment parameters, laser power and scanning speed, in computer software. The stage under the PDMS samples is fixed in the X and Y axis and can be adjusted in the Z axis. The variations of laser focal length which are adjusted by the Z axis cause the difference in byproducts' width and depth as shown in Figure 4. (b). The black color trench shapes are byproducts of SLP. Because the change in width and depth can cause the fluctuation of sensor performances, we have to prevent this phenomenon. Therefore, we fixed the laser focal length and thickness of PDMS to get consistent sensor performances. More specifically, we try to fix the defocusing length, 200um, from the tight focusing point and make precise samples based on the acrylic mold method.

## 2.3 Experiment Set-up for Sensor Applications

The experiment set-up is comprised as shown in Figure 5. (a), (b), and (c) to evaluate the performances of strain, temperature, and gas sensors.

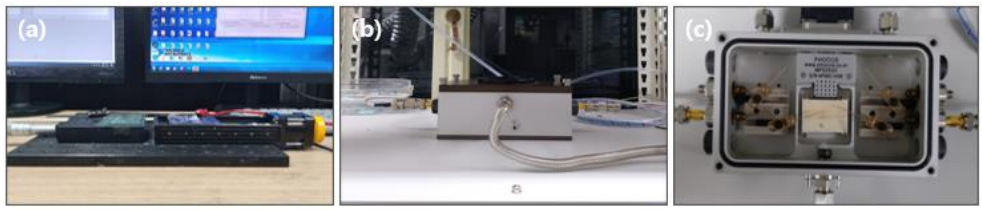


**Figure 5. Experiment set-up for (a) strain test. (b), (c) temperature and gas test.**

The strain stage shown in Figure 5. (a) can move 75mm back and forth. The chamber shown in Figure 5. (b), (c) has a heater capable of heating up to 200℃, and through lines, various gases such as $NO_2$, CO, $H_2S$, and $NH_3$ can flow into. Because the temperature of heater in the chamber can be programmed, temperature sensor experiments are progressed by changing temperature and measuring the variation of resistance. The gas sensor experiments are conducted in the 100℃ heater condition, which means the various gas flow into the chamber pre-heated 100℃ to accelerate the adsorption and desorption between byproducts and gases.

# Chapter 3. Byproduct Characterizations

We suggested the concept and preparation of process named SLP fabricating small line width under 10um on a transparent PDMS substrate in Chapters 1 and 2. In Chapter 3, byproduct characterization will be introduced. More specifically, the byproduct's shapes are analyzed using optical microscope (OM), scanning electron microscopy (SEM), and materials properties are investigated using ultraviolet-visible spectrophotometer (UV-VIS), X-ray diffraction (XRD), X-ray photoelectron spectroscopy (XPS), and Raman spectroscopy. As a result, a conclusion about hierarchical materials composition of byproducts will be suggested.

## 3.1 Width, Depth Dimension and Line Resistance

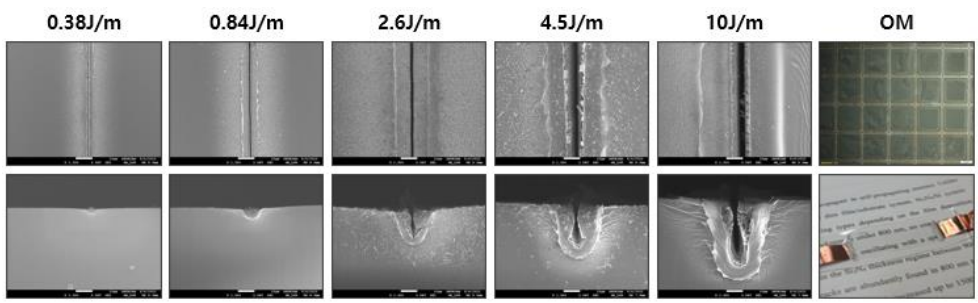


**Figure 6. Top and cross-sectional view SEM image of byproducts depending on laser energy density and OM image of fabricated sample.**

The width and depth of byproducts are investigated depending on laser energy density λ, which is given by: $\lambda=\rho/\nu$ where ρ is the laser power and ν is the laser scanning speed. Figure 6 shows the top and cross-sectional view of SEM image depending on laser energy density. Byproducts have a trench shape because the PDMS changed to CO gas which is blown away by laser pyrolysis. Trench shapes byproducts mean the path of thermal diffusion. Also, in 0.38J/m and 0,84J/m

conditions, the width of byproducts is confirmed as under 5um when we check the SEM images. It means that these widths are invisible and transparent to our naked eye.[24] The fabricated sample's transparency makes it possible to check the background letters when we confirm the OM result as shown in Figure 6.

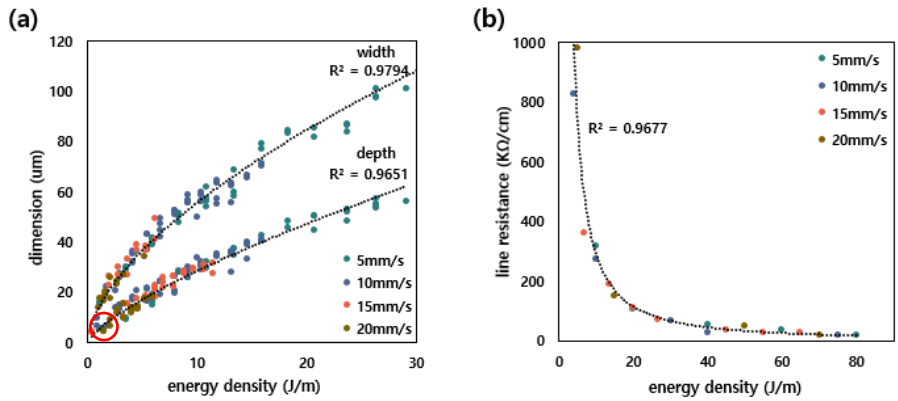


**Figure 7. (a) Width and depth of byproducts distribution depending on laser energy density. (b) Line resistance distribution depending on laser energy density.**

High reliability result about the byproducts' dimension of width and depth is derived as shown in Figure 7. (a). $R^2$, coefficient of determination, records 0.979 in width and 0.965 in depth according to laser energy density. It means width and depth have a significant correlation with laser energy density. Furthermore, line width under 5um can be fabricated as indicated in Figure 7. (a) red circle conditions. Figure 7. (b) shows the line resistances of byproducts depending on laser energy density. When we consider raw PDMS doesn't have electrical conductivity, the line resistance of byproducts is an interesting result. Because PDMS acquires electrical conductivity through SLP, byproducts can sense the type and size of external stimuli such as strain, temperature, and gas depending on the change of its initial resistance. Also, line resistance according to laser energy density records the $R^2$ value 0.967. It means there is a strong correlation between

line resistance and laser energy density.

## 3.2 UV-VIS Result of Byproduct

To investigate the transparency of byproducts quantitatively, we conducted the UV-VIS analysis. We mainly focus on the visible wavelength regions.

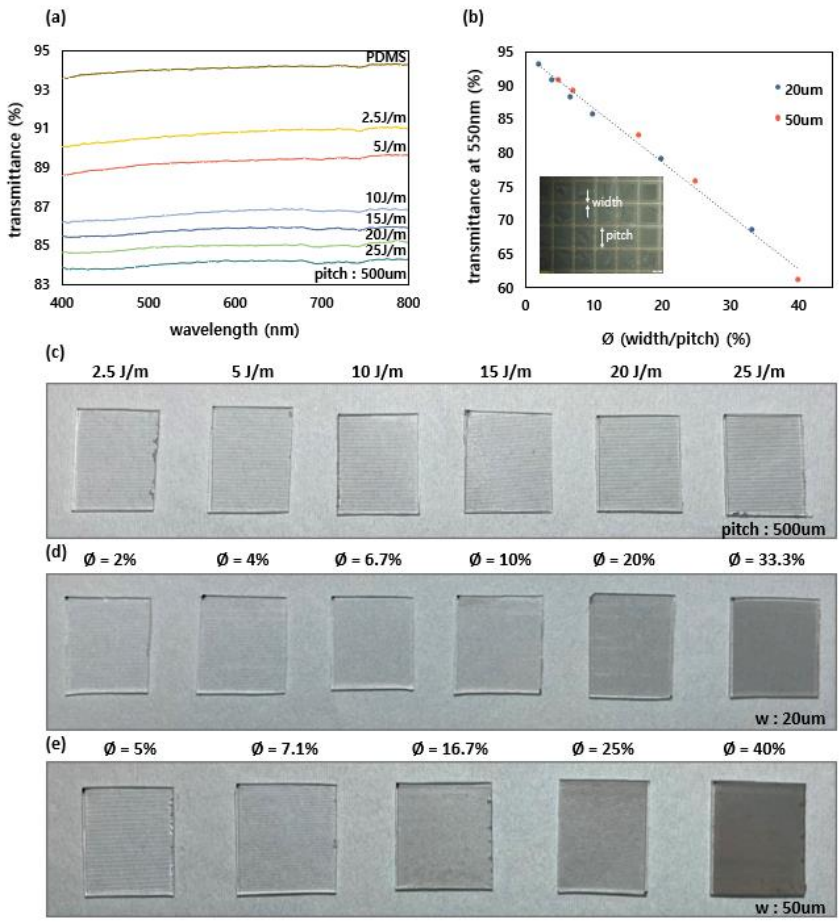


**Figure 8. (a) Transmittance of byproducts depending on laser energy density when pitch fixed to 500um. (b) Transmittance at 550nm of byproducts depending on Ø when width fixed to 20 and 50um. (c) Digital pictures of result (a). (d), (e) Digital pictures of result (b).**

Parameter pitch means the distance between lines fabricated by SLP. Figure 8. (a) shows the result of transmittances in the range of 400nm to 800nm depending on laser energy density. At this time, the pitch is fixed to 500um. In all conditions,

transmittances are over 83%, this means fabricated samples are greatly transparent. When we consider the transmittance at the visible wavelength range of polyimide which is widely used in LIG is 80%, the transmittances of all laser conditions are remarkable.[25] In conclusion, manufactured samples don't lose transparent property which is the intrinsic character of PDMS. Figure 8. (b) shows the transmittances depending on Ø, which is given by Ø=width/pitch. Width is fixed to 20 and 50um and pitch is changed to modulate Ø. We can confirm variation of Ø causes linear changes in transmittances. This means that we can control the degree of the samples' transparency. Figure 8. (c), (d), and (e) show the digital images of samples used in Figure 8. (a) and (b). We can directly recognize the difference in transparency between samples with the naked eye. The modulation of properties such as transmittance and emissivity from color change of samples can be applied in various research fields like radiative cooling.[26]

## 3.3 XRD, XPS, and Raman Spectroscopy Result of Byproduct

Byproducts of SLP are analyzed by XRD, XPS, and Raman spectroscopy.

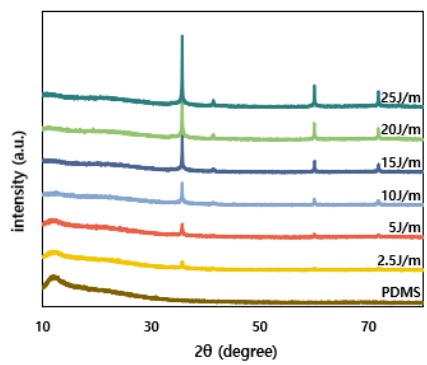


**Figure 9. XRD results of byproducts for various laser energy densities.**

Figure 9, the XRD results, revealed beta-SiC is generated by SLP when we check

the 35, 42, 60, and 72 peak degrees. Furthermore, when considering the intensity of XRD peaks, high crystalline beta-SiC can be fabricated when increasing laser energy density. When we contemplate that SiC is widely used in various research fields such as gas sensors and power electronics, SLP has a powerful advantage that can make beta-SiC an easy fabrication process at room temperature and atmosphere.[27] [28] Meanwhile, as will be mentioned later, carbon materials like graphite also exist in byproducts. However, the peak around 25 degree which means the existence of graphite doesn't appear in our XRD result. The reason for this issue will be explained in Chapter 3.4.

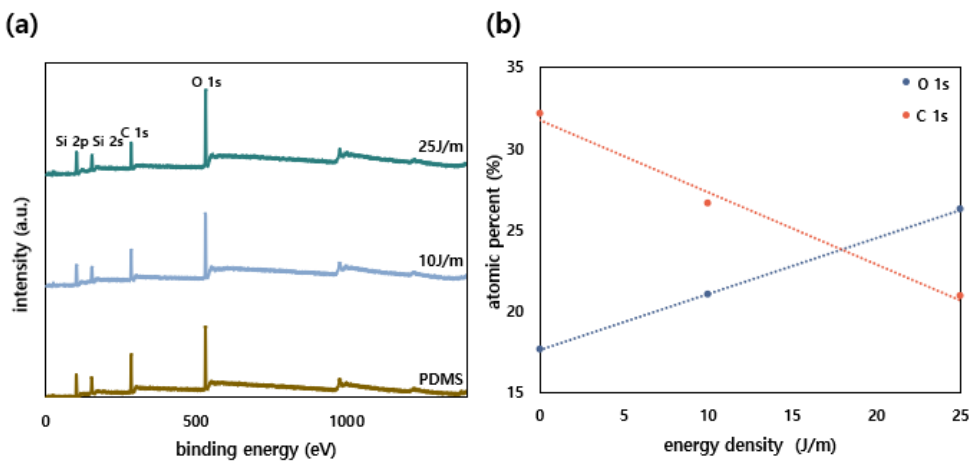


**Figure 10. (a) XPS results of byproducts for various laser energy densities. (b) Atomic percentage differences of C and O atoms depending on laser energy density.**

Through the XPS results as shown in Figure 10. (a), we can derive atomic percentage differences of C and O atoms depending on various laser conditions as shown in Figure 10. (b). Through this outcome, we can perceive more $SiO_2$ is formed according to higher laser energy density. Also, there is linear relationship between laser energy density and the atomic percent of C and O. Therefore, we can estimate the ratio of C, O, $SiO_2$, and beta-SiC in arbitrary conditions.

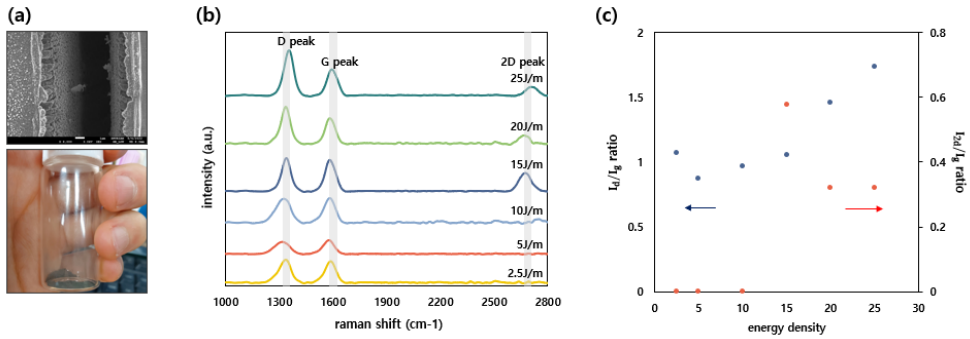


**Figure 11. (a) Sample images for Raman spectroscopy. (b) Raman spectroscopy results of byproducts. (c) Peak ratios of Raman spectroscopy results.**

Figure 11. (a) shows the sample image for Raman spectroscopy. We made byproducts to the powder-type samples because it is hard to tightly focus on the byproducts by visible laser of Raman spectroscopy. The reason for hard to focus is that the byproducts are highly porous. In all conditions, carbon D and G peaks appear as shown in Figure 11. (b), this means carbon materials such as graphite and graphene are formed. Furthermore, in the specific condition which is over 15J/m, the carbon 2D peak appears and this implies graphene is fabricated. But under 10J/m conditions, only carbon D and G peaks appear, and it means graphite is formed. Figure 11. (c) shows the peak intensity ratio $I_d/I_g$ and $I_{2d}/I_g$ according to laser energy density. Lower $I_d/I_g$ and higher $I_{2d}/I_g$ represent the lower defect level of carbon materials and higher graphene crystallinity respectively.[29] Through these data, we can recognize as the laser energy density increases, $I_d/I_g$ increases which means high-defect graphite is formed and $I_{2d}/I_g$ is decreased which means low-quality graphene is formed. As a result, when we consider $I_d/I_g$ and $I_{2d}/I_g$ peaks comprehensively, 15J/m conditions can be determined as an optimum condition. However, because the optimal condition can be changed depending on the type of external stimuli, we will use samples fabricated at various conditions when testing

as a sensor and examine performances.

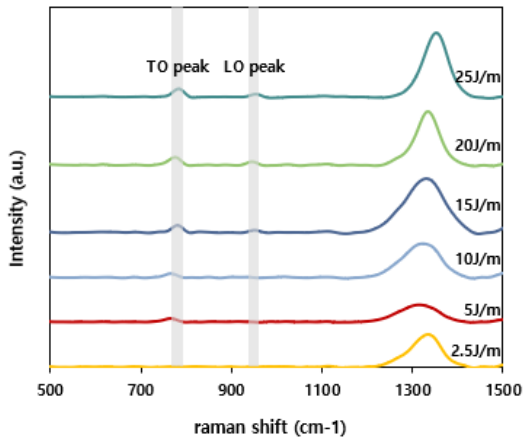


**Figure 12. Raman spectroscopy results of byproducts to explain the tendency of beta-SiC.**

Also, we can find Raman spectroscopy peaks composed of the transverse optical (TO) and longitudinal optical (LO) peaks that mean the existence of beta-SiC as shown in Figure 12.[30] However, it is hard to acquire these beta-SiC peaks because the quantity of beta-SiC is much smaller than in carbon materials. Therefore, estimating the tendency of beta-SiC formation through Raman spectroscopy results is difficult, but we can insist it is possible to confirm the presence of beta-SiC and carbon materials in byproducts as shown in Figure 12.

## 3.4 Characterization Conclusion

When we consider the fact that because the X-ray power of XPS is usually much lower than that of XRD, it is known that the penetration depth of XPS is about several nanometers and of XRD is about several micrometers.[31] Dealing with this conclusion and the result of Raman spectroscopy, the pyrolysis byproducts are produced from the trench in the order of $SiO_2$, beta-SiC, and carbon-based materials as shown in Figure 13. At this time, the colors of $SiO_2$, beta-SiC, and

carbon in Figure 13 are fake and we marked these colors to help comprehension. The sophisticated thickness calculation of $SiO_2$, beta-SiC, and carbon-based materials layers is needed in future research.

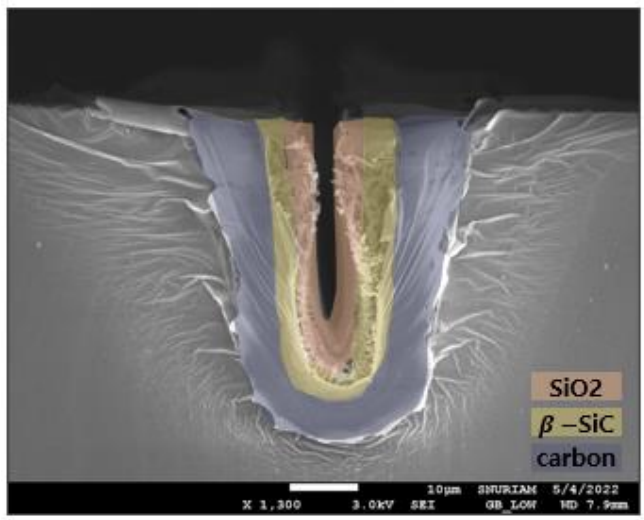


**Figure 13. Hierarchical composition of byproducts.**

This conclusion consists with the previous experiment.[32] In the previous study, researchers insist that a porous graphitic surface is integrated with SiC by showing high-angle annular dark-field scanning transmission electron microscopy (HAADF-STEM) image. Also, researchers show X-ray diffraction revealing a 3C polytype of SiC with stacking faults and graphite layer beneath. The difference in characterization results between our experiment and the previous study may have originated from laser power and speed. In our experiment, we utilized laser power between 20mW and 500mW and scanning speed between 5mm/s and 20mm/s. On the other hand, the previous study used 50W laser power and 0.254mm/s scanning speed. It means the laser energy density of the previous study is much higher than our conditions. Also, they used a $CO_2$ laser which has a different wavelength compared to our visible wavelength laser. We think huge laser energy density made

lots of graphite as byproducts and this phenomenon brought about results that graphite peak was recorded in XRD. To sum up our XRD, XPS, and Raman spectroscopy results, $SiO_2$, beta-SiC, and carbon materials are made sequentially from the trench and this conclusion matches with previous research.

# Chapter 4. Sensor Performance Test

In this chapter, reactions of byproducts against external stimuli such as strain, temperature, and gas are investigated. SLP byproducts are judged to be high-sensitivity sensors to external stimuli because of their high porosity and the existence of electrical conductivity. Furthermore, the result of sensing performance will be interpreted relating to the properties and compositions of byproducts. Lastly, the set-up for multiple stimuli experiments is comprised as shown in Figure 5.

## 4.1 Application as a Strain Sensor

First, we used byproducts fabricated at 5, 15, and 25J/m conditions as strain sensors to verify the performance tendency. Because byproducts are brittle, encapsulating the samples using PDMS is preceded when the strain sensing test progressed.

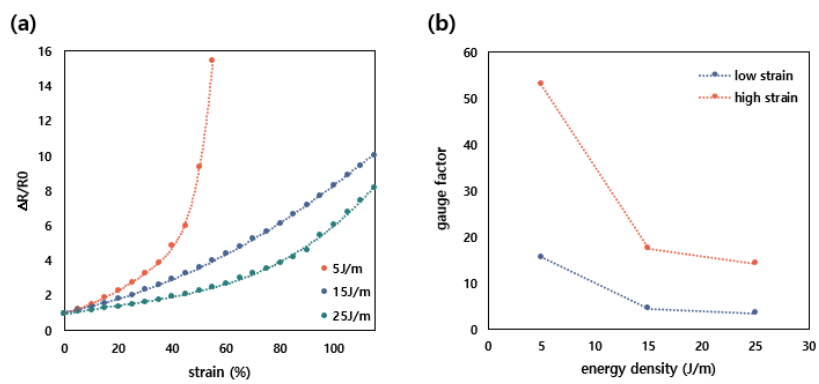


**Figure 14. (a) Strain response curve of byproducts depending on laser energy density. (b) Gauge factor (GF) at high and low strain.**

Figure 14. (a) shows the result of resistance change when strain is applied to the samples. It is notable that 5J/m byproducts show the highest sensitivity but can

maintain up to 50% strain. In the case of 15 and 25J/m samples, byproducts have relatively small sensitivity against strain but can keep up to 120% strain. As shown in Figure 14. (b), it is possible to check the GF, which is given by: GF=(ΔR/R)/ε where R is the initial resistance and ε is the applied strain. Through GF result, it is proved that 5J/m byproduct acquires the highest sensitivity at low and high strain. More specifically, 5J/m byproduct shows GF over 50 at high strain and over 15 at low strain. The reason why sensitivity of the strain sensors is inversely proportional to laser energy density is that brittle byproducts are fabricated when parameters related to power is lower.

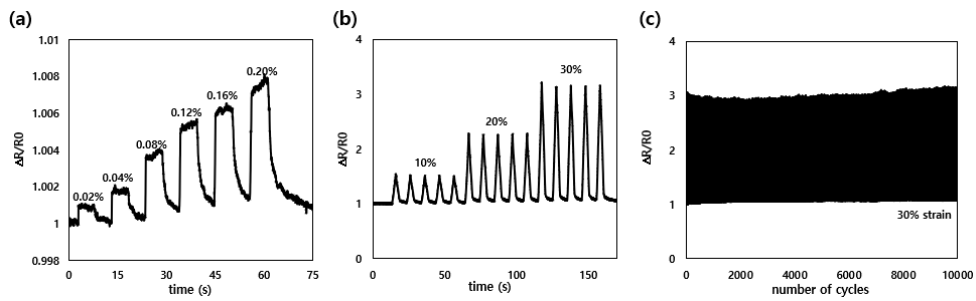


**Figure 15. (a) Minimum detectable strain of 5J/m sample. (b) Time dependent cyclic response of 5J/m sample. (c) Durability test of 5J/m sample at 30% strain.**

We used 5J/m sample byproduct, the highest sensitivity sensor, to measure various performances as a strain sensor. We measured minimum detectable strain, cyclic response against various strains, and durability. Figure 15. (a) shows that the sensor can detect a minimum of 0.02% strain. Furthermore, the sensor can perform well with no hysteresis at various conditions such as 10, 20, and 30% strain as shown in Figure 15. (b). At last, the sensor can endure 10,000 cycles of 30% strain as shown in Figure 15. (c), which means the sensor can be used for a long time. Chapter 4.1 suggests various properties as a strain sensor and through these, we can utilize this

sensor as a transparent wearable strain sensor for future technology like E-skin and soft robotics.

## 4.2 Application as a Temperature Sensor

Second, we used byproducts fabricated at 5, 10, 15, 20, and 25J/m conditions as temperature sensors to verify the performance tendency. We used a heater embedded in the gas chamber as shown in Figure 5. (c) to acquire responses against temperature.

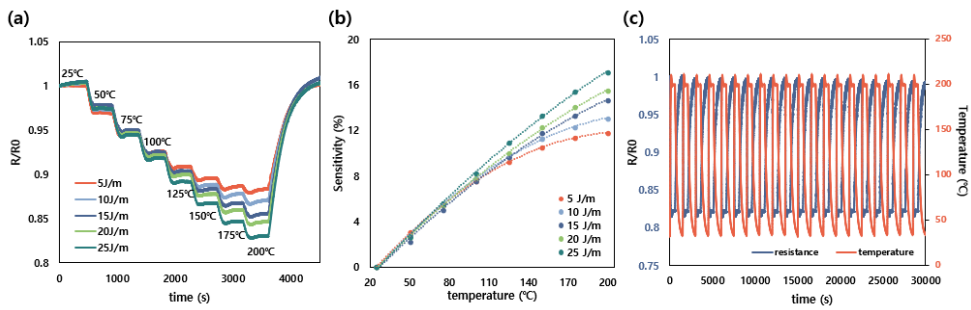


**Figure 16. (a) Temperature response curve of byproducts depending on laser energy density. (b) Sensitivity according to the temperature of fabricated sensors. (c) Durability test of 25J/m sample at cyclic conditions between 25 and 200℃.**

Figure 16. (a) shows the response curve of byproducts against external temperatures. When sensitivity is defined as the resistance change on the basis of initial resistance, the 25J/m sensor has the highest sensitivity according to temperature as shown in Figure 16. (b). We can verify the tendency of increasing sensitivity when the laser energy density is increasing. Also, it is important to find the reason for this tendency. The major reason for these phenomena is high crystalline beta-SiC is generated at high laser energy density as shown in the result of XRD. More specifically, because beta-SiC has a temperature coefficient resistance (TCR) value larger than graphite and graphene, it is possible to show a

huge resistance change in high laser energy density conditions in which more and the high crystalline beta-SiC can be formed.[33] [34] The sensor fabricated at 25J/m shows a resistance change of 0.102%/℃. At last, the test for measuring durability was progressed. Although PDMS has a thermal expansion coefficient of 310um/m℃, the 25J/m temperature sensor can perform well in cyclic conditions between 25 and 200℃ as shown in Figure 16. (c).[35] Because PDMS is widely used in organ-on-a-chip, bioengineering, medical devices, and stretchable electronics, the embedded temperature sensor in PDMS introduced in Chapter 4.2 will be utilized efficiently for various purposes.

## 4.3 Application as a Gas Sensor

Third, we used byproducts fabricated at 5, 15, and 25J/m conditions as $NO_2$ gas sensors to verify the various performances. We will examine the reaction between byproducts and $NO_2$ gas first and then check the responses against various gases like $NH_3$, $H_2S$, and CO. When we conduct the gas test, the external temperature is fixed at 100℃.

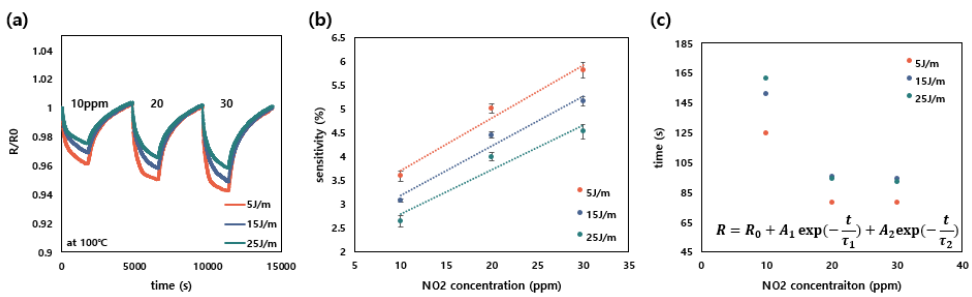


**Figure 17. (a) $NO_2$ gas response curve of byproducts depending on laser energy density. (b) Sensitivity of byproducts according to various concentrations of $NO_2$ gas. (c) Tim constant $\tau_1$ about $NO_2$ concentrations.**

Figure 17. (a) shows the response curves of 5, 15, and 25J/m sensors against $NO_2$ gas concentrations of 10, 20, and 30ppm. We can confirm the linear sensitivity of

the sensor to $NO_2$ gas concentrations in figure 17. (b) and 5J/m byproduct has the highest sensitivity. 5J/m sensor shows a 6% resistance change when it reacts with 30ppm $NO_2$ gas. 25J/m sensor shows the lowest sensitivity among various samples. The reason for this tendency is that the thickness difference of fabricated beta-SiC disturbs the reaction between the active layer composed of carbon materials and $NO_2$ gas. More specifically, in the 5J/m condition, the sensitivity against $NO_2$ is higher than 25J/m because the thickness of the beta-SiC layer is smaller than 25J/m. In general, beta-SiC is known to react with $NO_2$, but the scale of response is much smaller than that of graphite and graphene.[36] Therefore, we insist that 5J/m byproducts are more sensitive than 25J/m byproducts because beta-SiC is thinner in the 5J/m case. Time constant $\tau_1$ is acquired by fitting a two-phase exponential decay model as shown in Figure 17. (c). The exact equation of two-phase exponential decay model is in Figure 17. (c). When observing the obtained data, $\tau_1$ which is the time it took to 63.2% of fast decay phase is under 100 seconds when byproducts react with 20 and 30ppn $NO_2$. This result means byproducts can react with $NO_2$ gas fast enough. Especially, the 5J/m byproduct shows the smallest $\tau_1$ which is almost 70 seconds to 20 and 30ppm $NO_2$. Also, when we see the x-axis of Figure 17. (a) that is the $NO_2$ gas response curve of byproducts depending on laser energy density, the scale is of considerable size. It means that the response time between byproducts and $NO_2$ is huge. However, when we consider the time constant $\tau_1$, we can insist our samples' response is fast enough and don't need to observe a full response.

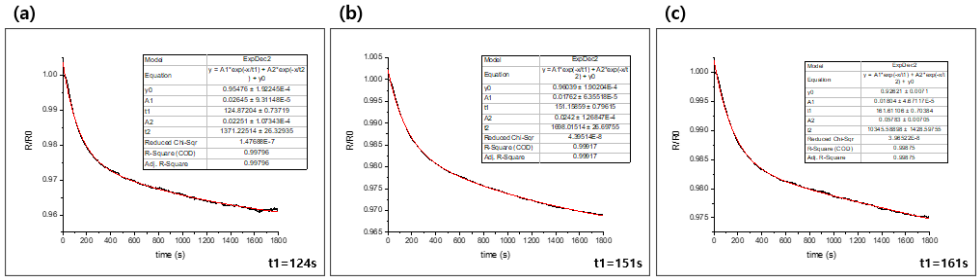


**Figure 18. Two-phase exponential decay model fitting curve between 10ppm $NO_2$ and (a) 5J/m byproducts, (b) 15J/m byproducts, and (c) 25J/m byproducts.**

Figure 18 shows the graph that solves the two-phase exponential decay model and acquires time constant $\tau_1$. Figure 18. (a), (b), and (c) describe the response curve and time constant between $NO_2$ 10ppm and 5J/m, 15J/m, and 25J/m samples respectively.

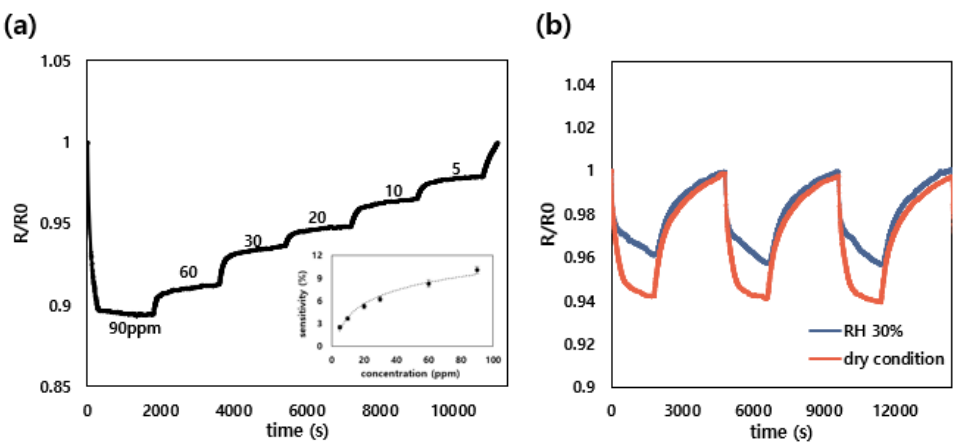


**Figure 19. (a) Response curve of 5J/m sensor to various $NO_2$ concentrations. (b) Response curve about with and without humidity.**

We utilize the 5J/m gas sensor which has the highest sensitivity to investigate various properties. The sensor shows the converging response when $NO_2$ concentration is increasing as shown in Figure 19. (a). Furthermore, to measure the reaction of the sensor in humidity conditions, we set relative humidity as 30%. The sensor operates well in 30ppm $NO_2$ concentration with and without humidity as

shown in Figure 19. (b). It is notable that when 30% relative humidity exists, the sensitivity is decreased slightly. We can know that the 5J/m sample is durable in repetitious 30ppm $NO_2$ conditions.

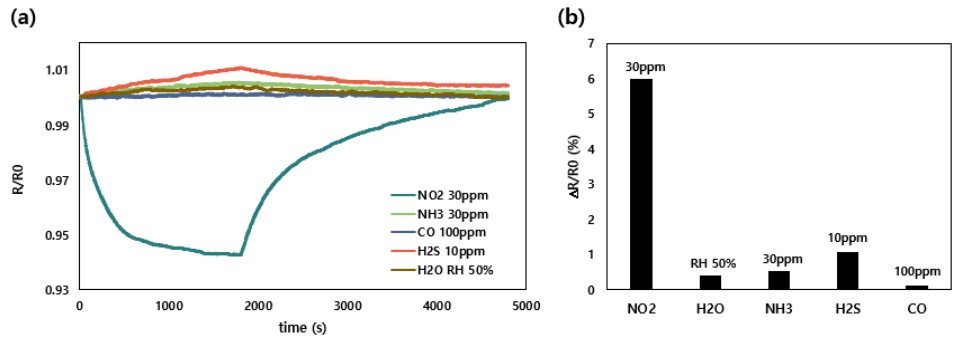


**Figure 20. (a) Full response curve between 5J/m byproducts and various gases. (b) The selectivity of $NO_2$ gas among various gases.**

At last, the selectivity of $NO_2$ gas among various gases such as $H_2O$, $NH_3$, $H_2S$, and CO is investigated. Figure 20. (a) shows the full responses between 5J/m samples and gases. It is notable that the response between byproducts and $NO_2$ gas is much larger than the others. Figure 20. (b) shows the result of $NO_2$ selectivity. Byproducts can selectively detect $NO_2$ among diverse gases and this is because of the existence of beta-SiC. The beta-SiC layer prevents the reaction between gases except of $NO_2$ and the sensing layer, graphite and graphene. So, the overall responses between carbon materials and gases are decreased slightly. At this time, because beta-SiC can adsorb $NO_2$ slightly, byproducts can detect only $NO_2$. Full response curve of our samples against various gases shown in Figure 20. (a) is similar to that of a single graphene layer.[37] It implies that components among our byproducts, carbon materials like graphite and graphene implement a major role when reacting with gases.

# Chapter 5. Conclusion

## 5.1 Summary of This Research

To fabricate transparent and multifunctional sensors in a simple process and break the limits of LIG process, we employed the SLP process. Through SLP, trench shape byproducts were formed. Properties such as width and depth were investigated using OM and SEM and line resistance was also explored. Through these processes, we verified the existence of line width under 5um and the possibility of using the byproducts as strain, temperature, and gas sensors. The transmittance of samples at the visible region is probed using UV-VIS and it showed over 80%. Furthermore, we inspected the hierarchical composition of byproducts using XRD, XPS, and Raman spectroscopy. Through this, we concluded the byproducts were composed of $SiO_2$, beta-SiC, and carbon materials. The composition ratio of byproducts can be modulated by controlling laser energy density. These ratio difference affects byproducts' response to strain, temperature, and gas. Based on these results, finally, we used the byproducts as strain, temperature, and gas sensors. As a strain sensor, the 5J/m byproduct showed the highest sensitivity and 25J/m byproduct showed the lowest sensitivity. This sensitivity variation occurs because of brittleness differences between samples. 5J/m sample could detect a minimum strain of 0.02% and endure 10,000 cycles of 30% strain. We verified this strain sensor can be used as a wearable mechanical sensor through experiment data. As a temperature sensor, the 25J/m byproduct showed the highest sensitivity because of its high crystalline beta-SiC and 5J/m byproduct showed the lowest sensitivity against external temperature. The

temperature sensor fabricated at 25J/m condition could endure repetitive temperature conditions between 25℃ and 200℃. At last, as a gas sensor, the 5J/m byproduct showed the highest sensitivity to $NO_2$, and 25J/m byproduct showed the lowest sensitivity. The reason of high sensitivity of 5J/m samples is its beta-SiC is thinner than others. Also, when we see the response time using the two-phase exponential decay model, time constant $\tau_1$ recorded under 100 seconds. We revealed that the 5J/m byproduct responds well to $NO_2$ in with and without humidity conditions. Finally, fabricated gas sensor had a high $NO_2$ selectivity among various gases such as $NH_3$, $H_2S$, and CO because beta-SiC thin film prevents the responses between carbon materials and various gases except $NO_2$.

## 5.2 Future Work

In this experiment, we examined the possibilities of SLP byproducts using as transparent and multifunctional sensors. We knew that fabricated sensors could detect external stimuli like strain, temperature, and gas well through data. The single sensor detected various stimuli like strain, temperature, and gas by resistance change which is a single signal. In future work, it is important to decouple the input single signal to know the type and size of stimuli that are exerted on the sensor. If this decoupling algorithm is realized, we can detect various stimuli in our real-life using a single sensor which operates with low power. Actually, some previous studies showed the possibilities of developing a decoupling algorithm and single sensor hardware. More specifically, research about separating the type and concentration of existing gas and quantity and wind speed of raindrops by one sensor are reported. [38] [39] [40] Researchers use advanced algorithms like deep-neural-network (DNN) and long-short-term memory (LSTM) to decouple multiple

data in one signal. Furthermore, it is important in future experiments to exactly investigate the response mechanism between pyrolysis byproducts and external stimuli like strain, temperature, and gas by using simulation programs, transmission electron microscope (TEM), atomic force microscopy (AFM), and BET measurement. Nowadays, PDMS polymer is used in various research fields such as bioengineering, microfluidic, soft-lithography technology, and sustainable energy application. We introduced in this experiment the technologies, successive laser pyrolysis of PDMS and using byproducts as a transparent and multifunctional sensor, and the implementation possibility of advanced software which decouples multiple stimuli and detects type and quantity of stimuli. We believe these technologies will be widely used in various fields of research mentioned above.

# Reference


[1] H. S. Jo, S. An, C.-W. Park, D.-Y. Woo, A. L. Yarin, S. S. Yoon, *ACS applied materials & interfaces* **2019**, 11, 40232.

[2] N. Jiang, D. Hu, Y. Xu, J. Chen, X. Chang, Y. Zhu, Y. Li, Z. Guo, *Advanced Composites and Hybrid Materials* **2021**, 4, 574.

[3] B. W. An, S. Heo, S. Ji, F. Bien, J.-U. Park, *Nature communications* **2018**, 9, 1.

[4] X. Ye, M. Qi, Y. Yang, M. Yu, T. Huang, J. Zhang, X. Yuan, G. Suo, X. Hou, L. Feng, *Advanced Materials Technologies* **2020**, 5, 2000446.

[5] S. Zhang, A. Chhetry, M. Zahed, S. Sharma, C. Park, S. Yoon, J. Y. Park, *npj Flexible Electronics* **2022**, 6, 1.

[6] Y. Rho, K. Lee, L. Wang, C. Ko, Y. Chen, P. Ci, J. Pei, A. Zettl, J. Wu, C. P. Grigoropoulos, *Nature Electronics* **2022**, 5, 505.

[7] D. Won, J. Kim, J. Choi, H. Kim, S. Han, I. Ha, J. Bang, K. K. Kim, Y. Lee, T.-S. Kim, *Science Advances* **2022**, 8, eabo3209.

[8] K. K. Kim, I. Ha, M. Kim, J. Choi, P. Won, S. Jo, S. H. Ko, *Nature communications* **2020**, 11, 1.

[9] J. Lin, Z. Peng, Y. Liu, F. Ruiz-Zepeda, R. Ye, E. L. Samuel, M. J. Yacaman, B. I. Yakobson, J. M. Tour, *Nature communications* **2014**, 5, 1.

[10] R. Ye, Y. Chyan, J. Zhang, Y. Li, X. Han, C. Kittrell, J. M. Tour, *Advanced Materials* **2017**, 29, 1702211.

[11] L. Cao, S. Zhu, B. Pan, X. Dai, W. Zhao, Y. Liu, W. Xie, Y. Kuang, X. Liu, *Carbon* **2020**, 163, 85.

[12] W. Song, J. Zhu, B. Gan, S. Zhao, H. Wang, C. Li, J. Wang, *Small* **2018**, 14, 1702249.

[13] A. Lamberti, F. Clerici, M. Fontana, L. Scaltrito, *Advanced Energy Materials* **2016**, 6, 1600050.

[14] S. Luo, P. T. Hoang, T. Liu, *Carbon* **2016**, 96, 522.

[15] A. Dallinger, K. Keller, H. Fitzek, F. Greco, *ACS applied materials & interfaces* **2020**, 12, 19855.

[16] M. G. Stanford, C. Zhang, J. D. Fowlkes, A. Hoffman, I. N. Ivanov, P. D. Rack, J. M. Tour, *ACS applied materials & interfaces* **2020**, 12, 10902.

[17] J. Shin, J. Ko, S. Jeong, P. Won, Y. Lee, J. Kim, S. Hong, N. L. Jeon, S. H. Ko, *Nature Materials* **2021**, 20, 100.

[18] B.-H. Jo, L. M. Van Lerberghe, K. M. Motsegood, D. J. Beebe, *Journal of microelectromechanical systems* **2000**, 9, 76.

[19] A. Mata, A. J. Fleischman, S. Roy, *Biomedical microdevices* **2005**, 7, 281.

[20] D. Qi, K. Zhang, G. Tian, B. Jiang, Y. Huang, *Advanced Materials* **2021**, 33, 2003155.

[21] G. Camino, S. Lomakin, M. Lageard, *Polymer* **2002**, 43, 2011.

[22] S. Arscott, *Journal of Micromechanics and Microengineering* **2020**, 30, 025003.

[23] T. Baëtens, S. Arscott, *Journal of Micromechanics and Microengineering* **2019**, 29, 115005.

[24] C. Pan, K. Kumar, J. Li, E. J. Markvicka, P. R. Herman, C. Majidi, *Advanced Materials* **2018**, 30, 1706937.

[25] B. Deng, S. Zhang, C. Liu, W. Li, X. Zhang, H. Wei, C. Gong, *Rsc Advances* **2018**, 8, 194.

[26] J. Lee, Y. Jung, M. Lee, J. S. Hwang, J. Guo, W. Shin, J. Min, K. R. Pyun, H. Lee, Y. Lee, *Nanoscale Horizons* **2022**, 7, 1054.

[27] S. Ji, Z. Zhang, F. Wang, *CES Transactions on Electrical Machines and Systems* **2017**, 1, 254.

[28] N. Wright, A. Horsfall, *Journal of Physics D: Applied Physics* **2007**, 40, 6345.

[29] M. Dresselhaus, A. Jorio, R. Saito, *Annu. Rev. Condens. Matter Phys.* **2010**, 1, 89.

[30] T. Koyanagi, M. Lance, Y. Katoh, *Scripta Materialia* **2016**, 125, 58.

[31] L. Gontijo, R. Machado, E. Miola, L. Casteletti, P. Nascente, *Surface and Coatings Technology* **2004**, 183, 10.

[32] V. Nair, J. Yi, D. Isheim, M. Rotenberg, L. Meng, F. Shi, X. Chen, X. Gao, A. Prominski, Y. Jiang, *Science advances* **2020**, 6, eaaz2743.

[33] A. R. M. Foisal, H.-P. Phan, T. Kozeki, T. Dinh, K. N. Tuan, A. Qamar, M. Lobino, T. Namazu, D. V. Dao, *RSC advances* **2016**, 6, 87124.

[34] T. Dinh, H.-P. Phan, D. V. Dao, P. Woodfield, A. Qamar, N.-T. Nguyen, *Journal of Materials Chemistry C* **2015**, 3, 8776.

[35] J. H. Lee, H. Ryu, T. Y. Kim, S. S. Kwak, H. J. Yoon, T. H. Kim, W. Seung, S. W. Kim, *Advanced Energy Materials* **2015**, 5, 1500704.

[36] M. W. Nomani, R. Shishir, M. Qazi, D. Diwan, V. Shields, M. Spencer, G. S. Tompa, N. M. Sbrockey, G. Koley, *Sensors and Actuators B: Chemical* **2010**, 150, 301.

[37] F. Schedin, A. K. Geim, S. V. Morozov, E. W. Hill, P. Blake, M. I. Katsnelson, K. S. Novoselov, *Nature materials* **2007**, 6, 652.

[38] S. Wakabayashi, T. Arie, S. Akita, K. Nakajima, K. Takei, *Advanced Materials* **2022**, 2201663.

[39] M. Kang, I. Cho, J. Park, J. Jeong, K. Lee, B. Lee, D. Del Orbe Henriquez, K. Yoon, I. Park, *ACS sensors* **2022**, 7, 430.

[40] L. Li, S. Zhao, W. Ran, Z. Li, Y. Yan, B. Zhong, Z. Lou, L. Wang, G. Shen, *Nature Communications* **2022**, 13, 1.

# 국문 초록

# 폴리디메틸실록산의 연속 레이저 열분해를 통한 투명 다기능 센서 구현

이재군

기계공학부

서울대학교 대학원

오늘날, 레이저 직접 패터닝 분야에 대한 연구는 상온, 상압에서 공정 진행이 가능한 용이성과 효율성 때문에 국소적, 가역적 레이저 도핑, 고분자의 상 분리, 나노 물질의 레이저 소결, 융삭 등 분야에서 널리 사용되고 있다. 레이저 직접 패터닝 분야 중 탄소가 풍부한 물질에 레이저를 조사하여 다공성, 높은 전기전도도 특성을 가지는 그래핀을 만드는 레이저 유도 그래핀 기술이 주목받고 있다. 생성되는 그래핀은 기계적 센서, 화학적 센서, 에너지 장치 등 분야에 널리 사용되고 있다. 그러나 레이저 유도 그래핀 기술은 선 폭의 해상도와 관련된 한계가 존재하며 투명한 목적으로 사용하기 위해서는 기판에 전사를 해야하는 추가 공정이 필요한 문제가 있다. 본 연구에서는 간단한 공정으로 레이저 유도 그래핀 기술의 한계를 극복할 수 있는 폴리디메틸실록산 물질의 연속 레이저 열분해 공정을 소개한다. 그리고 열분해 부산물을 이용하여 인장, 온도, 가스 자극에 반응하는 성능을 검토하고 레이저 유도 그래핀 물질의 대체 가능성을 확인하고자 한다. 최종적으로, 탄화규소, 이산화규소, 그래파이트, 그래핀으로 구성된 연속 레이저 열분해 부산물은 다양한 자극에 반응하는 투명 다기능 센서로 동작할 수 있고 앞으로 급격한 성장을 이룩할 유연한 전자기기, 신축성 전자기기의 발전에 기여할 것이다.

**주요어 :** 폴리디메틸실록산, 레이저 직접 패터닝, 레이저 열분해, 투명 센서, 다기능 센서

**학번 :** 2021-24532